

1 **Thermal stratification effects on flow over a generic urban**  
2 **canopy**

3 **V.B.L. Boppana · Z-T Xie · I.P. Castro**

4  
5 Received: date / Accepted: date

6 **Abstract** The influence of local surface heating and cooling on flow over urban-  
7 like roughness is investigated using large-eddy simulations (LES). By adjusting the  
8 incoming or outgoing heat flux from the ground surface, various degrees of local ther-  
9 mal stratification, represented by a Richardson number ( $Ri_\tau$ ), were attained. Drag and  
10 heat transfer coefficients, turbulence structure, integral length scales, and the strength  
11 of quadrant events that contribute to momentum and heat fluxes were obtained and  
12 are compared with locally stable, neutral and unstable flows. With increasing  $Ri_\tau$ , or  
13 equivalently as the flow characteristics change from local thermal instability to sta-  
14 bility, a gradual decline in the drag and heat transfer coefficients is observed. These  
15 values are found to be fairly independent of the type of thermal boundary condition  
16 (constant heat flux or constant temperature) and domain size. The maps of anisotropy  
17 invariants showed that for the values of  $Ri_\tau$  considered, turbulence structures are al-  
18 most the same in shape for neutral and unstable cases but differ slightly from those in  
19 the stable case. The degree of anisotropy is found to decrease as  $Ri_\tau$  increases from  
20  $-2$  to  $2.5$ . Compared to the neutral case, the integral length scales are shortened in  
21 the streamwise and vertical direction by ground cooling, but enhanced in the vertical  
22 direction with ground heating. Quadrant analysis showed that increase in floor heat-  
23 ing increases the strength of ejections above the canopy. However, the contributions  
24 of updrafts or downdrafts to heat flux are found not to be significantly influenced by  
25 the type of local thermal stratification for the values of  $Ri_\tau$  considered. The transport  
26 mechanisms of momentum and heat above the canopy are found to be very similar in  
27 both locally unstable and stable flows.

28 **Keywords** Correlations · Drag coefficient · Heat transfer coefficient · Quadrant  
29 events · Turbulent structures

---

V. B. L. Boppana · Zheng-Tong Xie · Ian P. Castro  
Faculty of Engineering and Environment  
University of Southampton  
Tel: +44(0)23 8059 2320  
Fax: +44(0)23 8059 3058  
E-mail: V.B.Boppana@soton.ac.uk

---

## 1 Introduction

Do the effects of thermal stratification have a dominant role on the structure of turbulence and mechanisms of pollutant transport in and above roughness canopies of various morphologies? To investigate this, numerous field, wind-tunnel and computational studies have been conducted, especially in the last two to three decades. The field studies included several vegetation (e.g. Gao et al., 1989) and urban (e.g. Christen et al., 2007) areas to understand the similarities and differences in the transport of momentum and heat over the two kinds of canopies. One of the similarities that was observed is that sweep events contribute most to the momentum flux below and immediately above the canopy height and ejection events dominate further above the canopy; these events are considered to be the signatures of the large coherent structures. Li and Bou-Zeid (2011) discussed in detail the dissimilarity of momentum, temperature and water vapour transport with increasing instability from measurements over a vineyard and a lake. However, it is difficult to obtain comprehensive, spatially detailed measurements from the field owing to instrument limitations and the impossibility of obtaining repeated and controlled conditions; wind-tunnel and computational studies can therefore be particularly useful.

The simplest geometry, yet challenging if thermal stratification is included, is two-dimensional (2-D) street canyons. Allegrini et al. (2013), Huizhi et al. (2003), Kovar-Panskus et al. (2002), for example, have studied such cases in wind tunnels and shown that surface heating greatly influences the number and intensity of vortices within the canyon. Similar observations have also been made from various computational studies (e.g. Cai, 2012; Kim and Baik, 1999; Park et al., 2012). In the case of 3-D roughness morphologies, by adjusting the temperatures of the approach flow and the floor of a wind-tunnel, Uehara et al. (2000) created a thermally stratified atmospheric boundary layer over square arrays of roughness obstacles. They showed that a stable atmosphere results in weak cavity eddies whilst unstable conditions enhances the strength of cavity eddies. Using LES, Inagaki et al. (2012) simulated a complete day time atmospheric boundary layer over a square array of cubes with ground and roof heating and showed that the turbulent organized structures above the canopy are correlated to the strong upward motion that occurs within the cavity of the arrays. All these ‘generic’ urban canopy investigations clearly imply that the dispersion of pollutants might be affected by surface heating. Computational studies on field sites like DAPPLE (Dispersion of Air Pollution and its Penetration into the Local Environment) have certainly suggested that weak unstable conditions in the approach flow have notable effects on scalar dispersion (Xie et al., 2013).

It is necessary to quantify the effects of such thermal stratification on street and/or neighborhood scale flows in order to provide required parameters for city or regional scale modelling. For this purpose, we first performed computations to simulate passive scalar dispersion from a surface area source in an array of uniform and random height blocks (Boppana et al., 2010), followed by simulation of heat transfer from the strongly heated leeward surface of a large building (Boppana et al., 2013). These computations showed good agreement with the wind-tunnel experiments of Pascheke et al. (2008) and Richards et al. (2006) respectively. The former LES study had no buoyancy and the latter included its effects on the surrounding flow. These previous

75 investigations led naturally to the current LES study where, instead of heating a single  
 76 surface of an isolated obstacle, the entire ground surface (i.e. all streets, in direct  
 77 contact with the atmosphere) is uniformly heated (see Fig. 1) or cooled and the re-  
 78 sulting buoyancy effects are included to model the flow over an array of staggered  
 79 cubes. It is to be noted that, in this study, thermal stratification in a fully-developed  
 80 boundary layer is a result of surface heating or cooling within the bottom canopy,  
 81 which is rather different to the case of a thermally stratified approach flow over an  
 82 unheated region (e.g. Xie et al., 2013).

83 The overall goal of the present paper is to obtain insights on the effects of uniform  
 84 ground heating or cooling on the flow over an array of uniform height staggered  
 85 buildings. To address this, the following objectives were formulated: (1) to quantify  
 86 the effects of thermal stratification on the surrounding flow, including the turbulence  
 87 structure, and (2) to determine the similarities and/or differences in momentum and  
 88 heat transport for stable, neutral and unstable stratified flows *via* assessment of the  
 89 affects of stratification on surface drag and heat transfer coefficients. We present the  
 90 numerical description in Sect. 2, followed by the results and conclusions in Secs. 3  
 91 and 4 respectively.

## 92 2 Numerical Details and Settings

93 The filtered continuity and Navier–Stokes equations governing unsteady incompress-  
 94 ible flow are

$$\frac{\partial u_i}{\partial x_i} = 0, \quad (1a)$$

95 and,

$$\frac{\partial u_i}{\partial t} + \frac{\partial u_i u_j}{\partial x_j} = -\frac{1}{\rho} \left( \frac{\partial p}{\partial x_i} + \delta_{i1} \frac{\partial \langle P \rangle}{\partial x_1} \right) + \frac{\partial}{\partial x_j} \left( \frac{\tau_{ij}}{\rho} + \nu \frac{\partial u_i}{\partial x_j} \right) + f \delta_{i3}. \quad (1b)$$

96 The resolved-scale velocity and pressure are respectively given by  $u_i$  and  $p$  with  $u$ ,  
 97  $v$  and  $w$  the streamwise, lateral and vertical velocity components respectively. The  
 98 flow was driven by a constant mean streamwise pressure gradient  $\partial \langle P \rangle / \partial x$  and  $\delta_{i1}$  is  
 99 the Kronecker-delta.  $f \delta_{i3}$  is the body force due to thermal buoyancy and is estimated  
 100 using the Boussinesq approximation.  $\rho$  and  $\nu$  are the density and kinematic viscosity  
 101 of the fluid.  $\tau_{ij}$  is the subgrid-scale (SGS) Reynolds stress and was handled using  
 102 the Smagorinsky model in conjunction with a Lilly damping function near the walls.  
 103 We set Smagorinsky’s constant  $C_s = 0.1$  since this was found to provide satisfactory  
 104 results in our earlier computations (Boppana et al., 2010).

105 In the streamwise ( $x$ ) and lateral ( $y$ ) directions, periodic boundary conditions were  
 106 employed. Stress free conditions were imposed on the top of the domain, i.e.,

$$\frac{\partial u}{\partial z} = \frac{\partial v}{\partial z} = 0; \quad w = 0. \quad (2)$$

107 No slip conditions were set on the bottom surface ( $z = 0$ ) and on all faces of the  
 108 roughness elements.

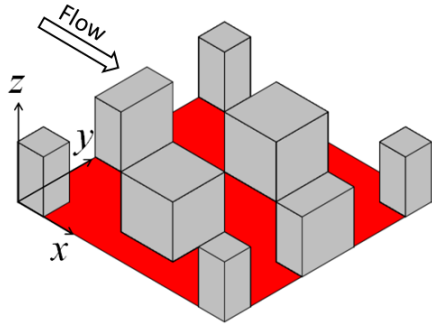


**Fig. 1** Sketch of 3-D view of computational domain. All the bottom surface between cubes is heated or cooled.

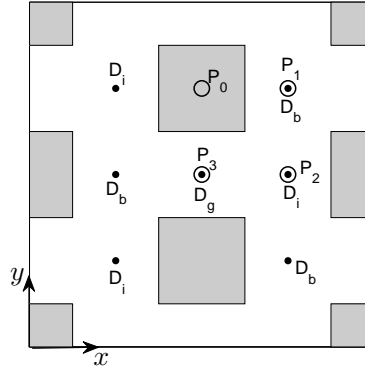


**Fig. 2** Plan view of computational domain. The four typical locations,  $P_{0-3}$  are identified by 'circles' and data at 'dots'  $D_b, D_i, D_g$  are used for quadrant analysis in Sect. 3.5.

109 The filtered governing equation for temperature is

$$\frac{\partial T}{\partial t} + \frac{\partial u_j T}{\partial x_j} = \frac{\partial}{\partial x_j} \left( (k_s + k_m) \frac{\partial T}{\partial x_j} \right), \quad (3)$$

110 where  $T$  is the resolved-scale temperature.  $k_s$  is the subgrid turbulent diffusivity and  
 111 is given by  $v_s/Pr_s$ , where  $v_s$  is the subgrid viscosity and  $Pr_s$  is the subgrid Prandtl  
 112 number whose value was set to 0.9.  $k_m$  is the molecular diffusivity and is defined  
 113 as  $v/Pr_m$ , where  $Pr_m$  is the molecular Prandtl number whose value was set to 0.71  
 114 in our computations. Periodic boundary conditions were specified in the streamwise  
 115 and spanwise directions. The stable stratification in the computational domain was  
 116 obtained by specifying a negative heat flux at the bottom surface and the same was  
 117 set to enter through the top surface. Similarly, the unstable stratification was obtained  
 118 by specifying a positive heat flux at the bottom surface of the computational domain  
 119 and the same was set to leave through the top surface. These computations were  
 120 done on a domain size of  $L_x \times L_y \times L_z = 4h \times 4h \times 6h$  (D4), where  $h = 0.2$  m is the  
 121 cube height. Whilst this domain is probably too small to capture adequately the long  
 122 streamwise rolls known to exist in the outer flow, earlier work has demonstrated that it  
 123 is sufficient for domain-independent mean flow fields, particularly within the canopy  
 124 region. For example, based on two-point measurements on an array of the same con-  
 125 figuration, Castro et al. (2006) showed that the integral length scales are constant in  
 126 the region  $2 \leq z/h \leq 4$  and are  $3h, 0.8h$  and  $h$  in  $x, y$  and  $z$  directions respectively.  
 127 Also, the DNS study by Coceal et al. (2006) showed that the mean flow field is in-  
 128 dependent of the domain sizes  $4h \times 4h \times 4h, 8h \times 8h \times 4h$  and  $4h \times 4h \times 6h$ . 3-D and  
 129 plan views of the computational domain are shown in Figs. 1 and 2 respectively. A  
 130 finite volume approach was followed to discretize the flow and temperature equa-  
 131 tions. The monotone advection and reconstruction scheme (STAR-CD, 2007) with a  
 132 blending factor of 0.9 was used for the spatial convective terms and the central differ-  
 133 ence scheme was used for the spatial diffusive terms of (1) and (3). A second-order

backward implicit scheme was used for discretizing the time-dependent term. The computational domain D4 consisted of hexahedral cells and the grid resolution was  $h/16$ . The driving force was the constant streamwise pressure gradient in Eq. (1) on every cell and is given by

$$\frac{\partial \langle P \rangle}{\partial x} = \frac{\rho u_\tau^2}{L_z} \quad (4)$$

where  $u_\tau$  is the total wall friction velocity. The Reynolds number ( $Re_\tau$ ) based on the total wall friction velocity and  $h$  was approximately 1200. The Reynolds number ( $Re$ ) based on  $h$  and the streamwise velocity at  $h$  varied from 3000 to 5000. The initial duration of most of the simulations was approximately  $200e_t$  where  $e_t = h/u_\tau$  is the eddy turn-over time. The averaging duration varied from  $200e_t$  to  $400e_t$  depending on how rapidly the shear and dispersive stresses converged. All the computations were carried out using STAR-CD version 4.14 (STAR-CD, 2007).

Sensitivity tests were done by conducting a further four independent sets of computations. They are

1. D4T - constant temperature instead of constant heat flux was specified on the top and bottom surfaces of the computational domain D4.
2. D4S - As an alternative means of achieving steady state for energy in the computational domain, constant heat sink (source) for unstable (stable) stratification was specified in all computational cells in D4 instead of a constant heat flux boundary condition on the top surface.
3. D16 - the domain size was  $8h \times 8h \times 10h$  with constant heat flux on the top and bottom surfaces of the domain. The vertical resolution varied geometrically from  $h/64$  at  $z = 0$  to  $h/16$  at the building height i.e  $z = h$ , and in the remaining parts of the domain  $h/16$  was used.
4. D64 - the domain size was  $16h \times 16h \times 10h$  with constant heat flux on the top and bottom surfaces of the domain. A uniform resolution of  $h/16$  was set throughout the domain.

A summary of all computations is given in Table 1.

### 3 Results

The first objective stated at the end of the Sect. 1 is addressed by determining the drag and heat transfer coefficients, displacement height  $d$  and roughness length  $z_0$  for various  $Ri_\tau$  in Sect. 3.1 and 3.2 respectively. By analysing the Reynolds stress anisotropy map, spatial correlations, quadrant and octant events for stable, neutral and unstable cases, the second objective is addressed and the details are presented in the latter subsections.

#### 3.1 Drag and heat transfer coefficients

The degree of thermal heating or cooling can be characterized by the Richardson number  $Ri_\tau$  defined as

$$Ri_\tau = \frac{gh(T_b - T_{z=0})}{T_b u_\tau^2} \quad (5)$$

Type of instability	Domain size	Type of thermal boundary condition	$q_{z=0}$ ( $\text{Wm}^{-2}$ ) or $T_{z=0}$ (K)	$Ri_\tau$	$C_d$	$C_h$
Stable	$4h \times 4h \times 6h$ (D4)	constant heat flux	-3	0.8775	0.0739	0.0066
			-8	2.5099	0.0645	0.0057
			-10	3.1986	0.0662	0.0057
			-12.5	4.1042	0.0628	0.0054
			-15	4.9978	0.0618	0.0053
			-18	6.1868	0.0569	0.0049
			-25	8.9943	0.0552	0.0046
Unstable	$4h \times 4h \times 6h$ (D4)	constant heat flux	1	-0.2737	0.0758	0.0071
			3	-0.7909	0.0779	0.0075
			8	-2.0472	0.0812	0.0079
			12.5	-3.0969	0.0856	0.0084
			25	-6.0259	0.0959	0.0091
			50	-11.6382	0.1158	0.0104
			100	-22.3893	0.1552	0.0125
Unstable	$4h \times 4h \times 6h$ (D4T)	constant temperature	293.35	-0.2703	0.0765	0.0072
			294	-0.7788	0.0796	0.0074
			297	-3.1465	0.0868	0.0084
			307	-11.0886	0.1155	0.011
Unstable <sup>a</sup>	$4h \times 4h \times 6h$ (D4S)	constant heat flux	3	-0.7343	0.0761	0.008
			8	-1.9416	0.0811	0.0083
Stable <sup>b</sup>	$4h \times 4h \times 6h$ (D4S)	constant heat flux	-8	2.0722	0.0688	0.0072
			-12.5	3.2955	0.064	0.0068
Unstable	$8h \times 8h \times 10h$ (D16)	constant heat flux	8	-1.504	0.0791	0.0106
			25	-4.1804	0.0862	0.0125
Unstable	$16h \times 16h \times 10h$ (D64)	constant heat flux	3	-0.75	0.0814	0.0081
			8	-1.9387	0.0817	0.0084
Neutral	D4	-	-	0	0.0759	-
	D16	-	-	0	0.0762	-
	D64	-	-	0	0.0816	-

**Table 1** Summary of computational cases.

a – To establish a steady state for energy, constant heat sink is specified throughout the domain.

b – To establish a steady state for energy, constant heat source is specified throughout the domain.

171 where  $g$  is the acceleration due to gravity and  $T_b$  is the bulk temperature, which is the  
172 average temperature over the whole domain. It is to be noted that  $Ri_\tau$  is not known *a*  
173 *priori*, but is an outcome of the computation that depends on the specified boundary  
174 conditions. The values of  $Ri_\tau$  along with the resulting coefficients are listed in Table 1.  
175 Instead of using the bulk or gradient Richardson numbers to represent the degree of  
176 thermal stratification, a frictional Richardson number is used here because the former  
177 two depend on domain size and particularly good accuracy in determination of the  
178 flux gradients, respectively. In the conventional definition of  $Ri_\tau$ , which is often used  
179 in (open) channel flows (e.g. Armenio and Sarkar, 2002; Dong and Lu, 2005; García-  
180 Villalba and del Álamo, 2011), the density or temperature difference between the two  
181 surfaces and channel half height are used. This definition is modified here for two  
182 reasons: (i) because a roughness height is a more appropriate characteristic length  
183 and (ii) similar to the bulk velocity, temperature distribution inside the domain also  
184 depends on domain height. Therefore, the temperature difference between the ground  
185 surface and bulk temperature instead of that at the top surface is used.

186 The thermal impact on the surrounding flow can be quantified using drag ( $C_d$ )  
 187 and heat transfer ( $C_h$ ) coefficients defined here as

$$C_d = \frac{u_\tau^2}{u_{z=h}^2} \quad (6)$$

188

$$C_h = \frac{q_{z=0}}{c_p \rho u_{z=h} (T_b - T_{z=0})} \quad (7)$$

189 where  $c_p$  is the specific heat capacity at constant pressure and  $q_{z=0}$  is the heat flux  
 190 at the ground surface. Note that when constant heat flux was specified on the bottom  
 191 surface,  $T_{z=0}$  is the spatially and temporally averaged non-uniform surface tempera-  
 192 ture. Similarly when constant temperature was specified on the ground surface,  $q_{z=0}$   
 193 is the spatially and temporally averaged non-uniform surface heat flux. The procedure  
 194 for obtaining  $T_{z=0}$  or  $q_{z=0}$  (STAR-CD, 2007) was as follows:

$$T^+ = \begin{cases} Pr_m z^+ & \text{if } z^+ \leq z_T^+ \\ (Pr_s + Pr_m)(u^+ + P) & \text{if } z^+ > z_T^+ \end{cases} \quad (8)$$

195 where

$$T^+ = \frac{c_p \rho (T_{z=0} - T_{z_1}) u_*}{q_{z=0}} \quad (9)$$

196 and

$$u^+ = \begin{cases} z^+ & \text{if } z^+ \leq z_u^+ \\ \frac{1}{\kappa} \ln(E z^+) & \text{if } z^+ > z_u^+ \end{cases} \quad (10)$$

Here  $z^+ = z_1 u_* / \nu$ ,  $T_{z_1}$  is the temperature at the near-wall grid point,  $z_1$  is the distance  
 from the wall to the centre of the near-wall grid point,  $u_*$  is the near-wall friction  
 velocity determined by Spalding's law (Shih et al., 1999) and  $P$  is the sub-layer resis-  
 tance factor (Jayatilaka, 1969).  $z_u^+$  and  $z_T^+$  satisfy the following equations:

$$z_u^+ - \frac{1}{\kappa} (E z_u^+) = 0 \quad (11)$$

$$Pr_m z_T^+ - (Pr_s + Pr_m) \left[ \frac{1}{\kappa} \ln(E z_T^+) + P \right] = 0 \quad (12)$$

197 where  $E$  is an empirical coefficient whose value was set to 9. It was observed in our  
 198 computations that most of the near-wall grid points lie within the viscous sublayer.

199 For the basic case, D4, Figs. 3a and b show an increase in  $C_d$  and  $C_h$  as the  
 200 thermal stratification changed from stable to unstable. For  $Ri_\tau < 0$ , a similar increas-  
 201 ing trend was also found by Cheng and Liu (2011) and Kanda et al. (2007) in 2-D  
 202 street canyons and the COSMO (Comprehensive Outdoor Scale Model) experiments  
 203 respectively. Such an increase is due to a gradual increase in the strength of the tur-  
 204 bulence motions, as illustrated by the data in Fig. 8a (discussed later). In comparison  
 205 with the flow over smooth terrain, stability effects on the flow over a rough surface  
 206 are likely to be lower because of the dominant influence of the mechanical turbulence  
 207 generated by the roughness elements. However, the assumption that urban flows may  
 208 be considered as neutral or nearly neutral in urban dispersion models (Britter and  
 209 Hanna, 2003) is probably invalid, as the results presented above suggest that stratifi-  
 210 cation effects are not negligible.

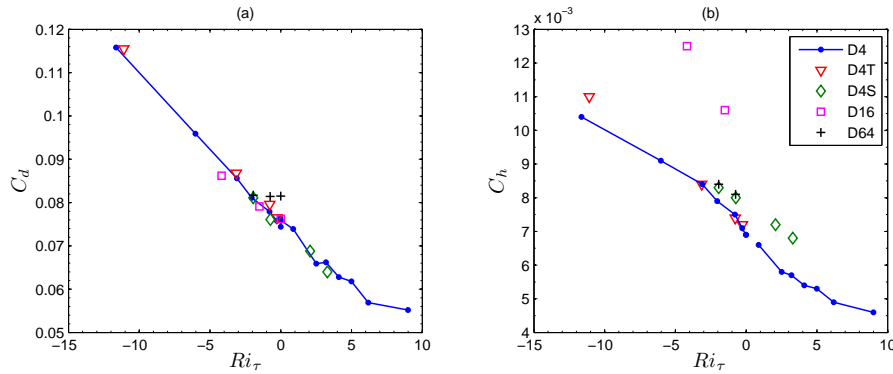


**Fig. 3** Variation of (a)  $C_d$  and (b)  $C_h$  with  $Ri_\tau$ . For the legend details, see Table 1.

### 211 3.1.1 Sensitivity checks

212 As mentioned in Sect. 2, the sensitivity tests were done by performing computations  
 213 on different domain sizes and grid resolution. In Figs. 3a and b, the values of  $C_d$  and  
 214  $C_h$  from D16 and D64 are also shown. It can be observed that  $C_d$  from D4 and D16  
 215 are in good agreement. Both D4 and D16 show gradual increase in  $C_d$  with  $Ri_\tau$ , while  
 216 the drag coefficient from D64 remains constant as  $Ri_\tau$  decreases from 0 to  $-1.94$  but  
 217 is anyway quite close to the results from the smaller domains. Figure 3(b) shows that  
 218 the values of  $C_h$  from D64 are approximately 7% larger and those from D16 are ap-  
 219 proximately 41% larger than D4. The significant increase seen in D16 can perhaps be  
 220 partly attributed to domain size effects but, much more importantly, is a direct result  
 221 of the much finer resolution near the ground surface. Although we have shown that  
 222 it is necessary to employ fine resolution near the surface to predict scalar transfer co-  
 223 efficients very accurately (Boppa et al., 2010), to save on expensive computational  
 224 time (which would be particularly demanding for D64) an identical uniform resolu-  
 225 tion of  $h/16$  was enforced in all D4 and D64 cases. These computations show that  
 226  $C_d$  is fairly insensitive to both domain size and resolution but the estimation of  $C_h$  is  
 227 indeed significantly affected by the mesh resolution. Therefore, the variation of  $C_h$   
 228 with  $Ri_\tau$  shown here should be considered as a qualitative indicator only.

229 Figures 3a and b also show that the two types of thermal boundary conditions, i.e  
 230 constant heat flux (D4) and constant temperature (D4T) on bottom and top surfaces  
 231 of the computational domain, yield very similar values of  $C_d$  and  $C_h$ . Even though  
 232 a constant heat flux (temperature) boundary condition at the bottom of a rough wall  
 233 yields a non-uniform distribution of temperature (heat flux) around the obstacles,  
 234 this study confirms that the integral quantities are not significantly affected by the  
 235 different physics at the ground surface.

236 To establish a steady state for energy, all D4 unstable (stable) computations had  
 237 constant heat flux entering (leaving) through the ground surface and leaving (en-  
 238 tering) through the top surface of the computational domain. But this can also be  
 239 achieved by specifying constant sink (source) in all cells of the computational domain  
 240 for unstable (stable) cases and these simulations are classified as D4S. The differences



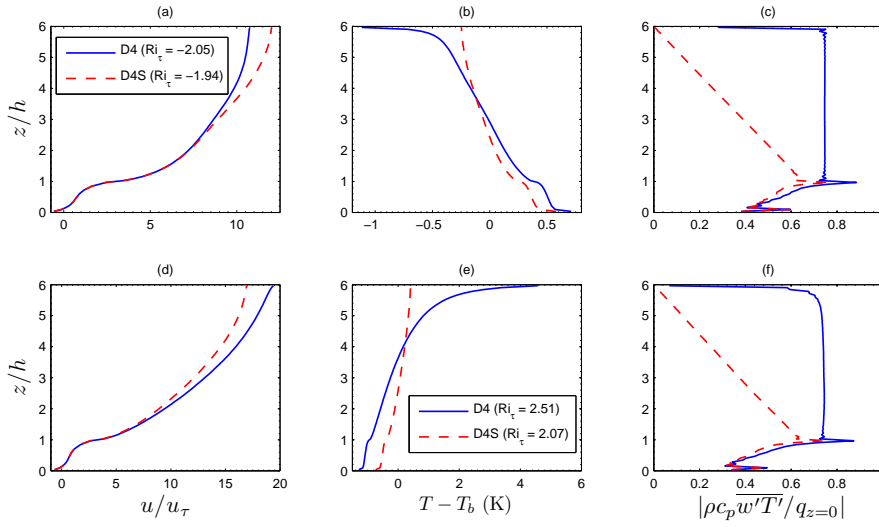


**Fig. 4** Comparison of temporally and spatially averaged profiles of (a & d) normalized streamwise velocity, (b & e) temperature difference and (c & f) normalized vertical turbulent heat flux for D4 and D4S. Top row: unstable, bottom row: stable. For the legend details, see Table 1.

241 in the vertical distribution of turbulent heat flux for D4 and D4S are shown in Fig. 4c  
 242 for both stable and unstable cases. Figure 3a shows that the drag coefficient is not  
 243 affected by the way in which steady state for energy is achieved, but the values of  $C_h$   
 244 from D4S in Fig. 3b are found to be 25% larger than in D4 for the stable case, while  
 245 only 5% larger in the unstable case. The reason for such differences can be explained  
 246 from the temporal and spatial mean of the temperature difference, shown in Fig. 4b. It  
 247 can be observed that the temperature variation with height is very much dependent on  
 248 the way in which steady state for energy is achieved. This in turn affects the flow field  
 249 and can be seen in the spatial and temporal mean profiles of streamwise velocity in  
 250 Fig. 4a. This brief numerical test suggests that heat transfer coefficients are sensitive  
 251 to the way in which steady state for energy in the computational domain is realised.  
 252 It would be quite challenging if not impossible to set up heat sinks or sources away  
 253 from boundaries in a wind-tunnel experiment, and in any case such sources or sinks  
 254 are not possible physically without the action of additional flow variables, like mois-  
 255 ture content. Further analysis in this current study is therefore restricted to cases with  
 256 constant heat flux boundary conditions on the top and bottom surfaces.

### 257 3.1.2 A note on domain size and its influence on dispersive stresses

258 Dispersive stresses, denoted by  $\langle \widetilde{uw} \rangle$  in the case of shear stress, arise due to spatial  
 259 inhomogeneities in the flow. Therefore, their presence is expected below the canopy  
 260 but not far above. In the case of D4, the dispersive stresses above the canopy were  
 261 very small. But in the case of D64, it was observed that the dispersive stresses above  
 262 the canopy persisted even after a time average duration of  $1000e_t$ . This is because  
 263 D64 is conducive to the development of streamwise rolls that are larger in scale than

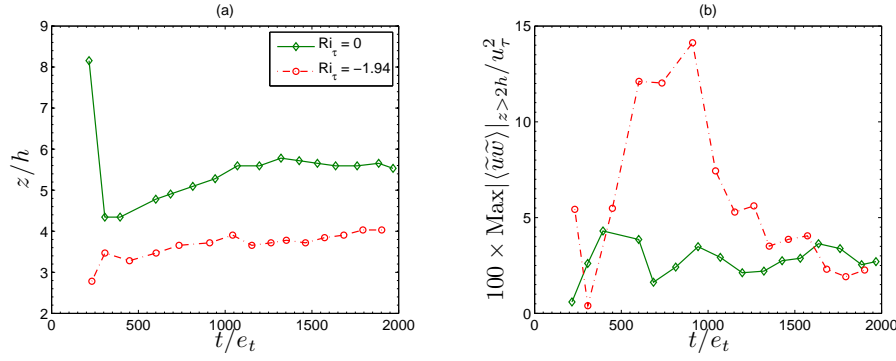


**Fig. 5** (a) Location of maximum dispersive stress and (b) percentage variation of maximum dispersive stress with time mean duration. The initial duration for  $Ri_\tau = 0$  and  $-1.94$  are  $200e_t$  and  $400e_t$  respectively.

264 are allowed by domain D4. Such slow evolving mean longitudinal rolls are clearly  
 265 shown in the DNS study of Coceal et al. (2006) for the neutral case. But it was  
 266 also shown that for a sufficiently long averaging time i.e.  $400e_t$ , these dispersive  
 267 stresses above the canopy disappear. It was observed in the current study that the  
 268 dispersive stresses above  $z/h = 2$  exhibit non-monotonic behaviour with increasing  
 269 averaging time. This can be seen in Fig. 5b, where the percentage variation with  
 270 averaging time of maximum dispersive stress for  $z > 2h$  is shown. It can be observed  
 271 that the maximum dispersive stress above the canopy appears to be converging to  
 272 approximately 2.5% of the wall stress (or approximately 5% of the shear stress at  
 273 that height) and the location at which it occurs is around  $z/h = 5.5$  and 4 for neutral  
 274 and unstable cases respectively. In a systematic set of investigations conducted by  
 275 Fishpool et al. (2009) in a turbulent channel flow at  $Re_\tau = 410$ , it was observed that  
 276 (i) the spanwise inhomogeneities persisted even when the domain length was increased  
 277 from  $2\pi\delta$  to  $62\delta$ , where  $2\delta$  is the channel depth and (ii) these features remained, with  
 278 a large magnitude, for time averaging in excess of  $10\delta/u_\tau$  (Fishpool et al., 2009,  
 279 called  $\delta/u_\tau$  the ‘friction time scale’). Detailed investigations are being carried out on  
 280 D64 to determine the averaging time required for the dispersive stresses to completely  
 281 disappear (if they do) and the reason for their existence over long durations.

### 282 3.2 Determination of pressure distribution, $d$ and $z_0$

283 It was observed in Sect. 3.1 that the increase in the drag coefficient with decreasing  
 284  $Ri_\tau$  is correlated with an increase in the turbulent kinetic energy. More directly,  
 285 however, it is the pressure difference between the windward and leeward sides of the  
 286 cubes which determine the (form) drag. The vertical profiles of time- and laterally-  
 287 averaged pressure coefficients ( $C_p$ ) were obtained for various  $Ri_\tau$  and are shown in  
 288 Fig. 6a. The pressure coefficient is defined as

$$C_p = \frac{(p_w - p_l)}{\frac{1}{2}\rho u_{z=h}^2}, \quad (13)$$

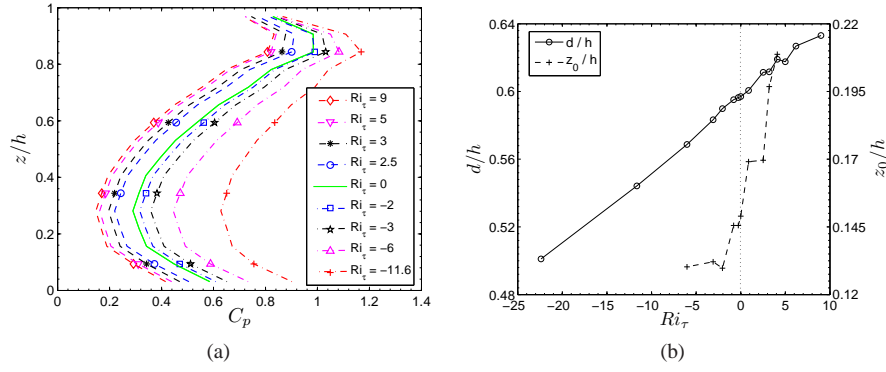


**Fig. 6** Variation of (a) temporally and laterally averaged normalised pressure coefficient, and (b) mean displacement height and roughness length with  $Ri_\tau$ .

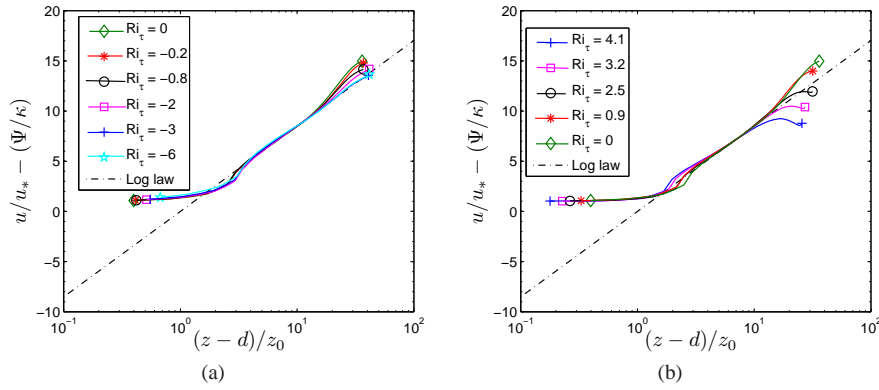


**Fig. 7** Spatial- and temporal-averaged mean streamwise velocity profiles in log-linear form for various  $Ri_\tau$  (a) neutral and unstable flows (b) neutral and stable flows.

289 where  $p_w$  and  $p_l$  are the pressures on the windward and leeward faces of the cube  
 290 respectively. It can be observed that there is a notable increase in the values of  $C_p$  with  
 291 ground heating and a slow decrease with ground cooling. The form drag,  $C_{pd}$ , can be  
 292 obtained by integrating Eq. 13 with respect to  $z$ , and in all cases is approximately 85%  
 293 of  $C_d$ . (The remaining drag component arises from frictional forces on the ground and  
 294 the top and sides of the cubes, see Leonardi and Castro (2010) for a discussion on this  
 295 point.)

296 The most sensible definition of the zero plane displacement height,  $d$ , is that it  
 297 is the height at which the surface drag acts (Jackson, 1981). Assuming that frictional  
 298 forces are negligible, this can be written (Coceal et al., 2006) as,

$$d = \frac{\int_z z(p_w - p_l)dz}{\int_z (p_w - p_l)dz}. \quad (14)$$

299 With the data shown in Fig. 6a this suggests that  $d$  decreases with increase in heating,  
 300 as confirmed in Fig. 6b. Although the change only amounts to some 25% over the

301 range of  $Ri_\tau$  covered, one would expect corresponding, but larger, changes in the  
 302 roughness length  $z_0$ , which was indeed found to be the case and can be seen in Fig. 6b.  
 303 The procedure of obtaining  $z_0$  at various  $Ri_\tau$  is briefly described below.

304 The wind speed profile for non-neutral condition is given by (Stull, 2009):

$$\frac{u}{u_*} = \frac{1}{\kappa} \left[ \ln \left( \frac{z-d}{z_0} \right) + \Psi \left( \frac{z-d}{L} \right) \right], \quad (15)$$

305 where  $\kappa$  is von Kármán's constant and  $L$  is the Obukhov length defined as

$$L = - \frac{\left[ \overline{u'w'^2}_{z=0} + \overline{v'w'^2}_{z=0} \right]^{3/4}}{\kappa (g/\overline{T}_v) (\overline{w'T'_v})_{z=0}} \equiv - \frac{u_*^3}{\kappa (g/\overline{T}_{z=0}) (q_{z=0}/\rho c_p)}. \quad (16)$$

306 Here primed quantities denote deviation from their respective mean values,  $\overline{T}_v$  is  
 307 mean virtual potential temperature and  $\overline{w'T'_v}$  is the mean kinematic virtual potential  
 308 temperature flux in the vertical direction. The stability function  $\Psi((z-d)/L)$  is typ-  
 309 ically given as (Stull, 2009)

$$\Psi \left( \frac{z-d}{L} \right) = \begin{cases} 4.7(z-d)/L & \text{for } Ri_\tau > 0 \\ -2 \ln \left[ \frac{1+\gamma}{2} \right] - \ln \left[ \frac{1+\gamma^2}{2} \right] + 2 \tan^{-1}(\gamma) - \frac{\pi}{2} & \text{for } Ri_\tau < 0, \end{cases} \quad (17)$$

310 where

$$\gamma = \left[ 1 - \zeta \frac{z-d}{L} \right]^{1/4} \quad \text{where } \zeta = 15. \quad (18)$$

311 In Eq. 15,  $\Psi = 0$  yields the standard logarithmic law for neutral (rough-wall) flow,  
 312 with  $u_*$  the surface friction velocity. (Note that the addition of the non-neutral term  
 313 ( $\Psi$ ) in Eq. 15 breaks the usual monotonic correspondence between  $z_0$  and  $u_*$ , so that  
 314 for  $Ri_\tau \neq 0$   $z_0$  may rise when  $u_*$  falls or *vice versa*.) For a pressure-driven channel flow  
 315 Coceal et al. (2006) derived  $u_* = u_\tau \sqrt{(1-d/L_z)}$  to account for the linear variation  
 316 in shear stress from  $z/h = d$  to  $L_z$  which otherwise is constant in the surface layer of  
 317 the atmospheric boundary layer.  $\zeta$  in Eq. 18 is changed to 16 such that the resulting  
 318  $\Psi$  agreed with that given in Table 1.1 of Kaimal and Finnigan (1994).

319 Using  $d$  from Eq. 14, the values of  $\kappa$  and  $z_0$  are obtained as fitting parameters of  
 320 Eq. 15 for neutral flow. The necessary value of  $\kappa$  was found to be 0.27, which is 34%  
 321 lower than the classical value of 0.41. A similar discrepancy from the classical value  
 322 was also reported by Cheng and Castro (2002), Coceal et al. (2007), Leonardi and  
 323 Castro (2010) to name a few.

324 By fixing  $\kappa$  as 0.27 and using the computed value of  $d$  for each  $Ri_\tau$ ,  $z_0$  was  
 325 deduced by fitting the measured  $u$  profile to Eq. 15 over a height range of  $z/h = 1.5$   
 326 to 2.5 - approximately chosen such that the variations of individual estimates of  $z_0$   
 327 from the velocity at a specific height in this range was less than 10%. However, for  
 328  $Ri_\tau < -6$  and  $> 4.1$ , the variation of  $z_0$  in the above mentioned range of  $z/h$  exceeded  
 329 10% and hence these data are not included in Fig. 6b.

330 Figure 7 shows the vertical variation of spatial- and temporal-averaged velocity  
 331 profiles for neutral, stable and unstable cases. It can be observed that the LES data is  
 332 not incompatible with the log-linear form and that for increasing  $|Ri_\tau|$  the data appear  
 333 to shift gradually to the right of the neutral case; this movement is found to be slightly  
 334 stronger in stable flows.

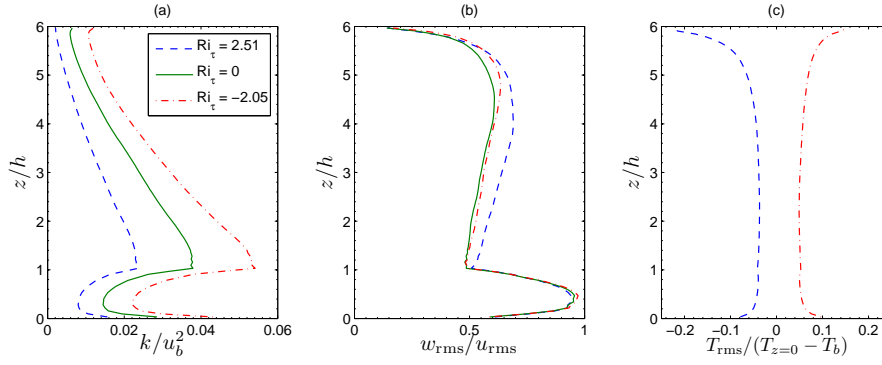


**Fig. 8** Temporal and spatial mean of (a) turbulent kinetic energy normalized with bulk velocity, (b) ratio of vertical to streamwise Reynolds stresses and (c) normalized temperature fluctuations for  $Ri_\tau \approx -2, 0$  and  $2.5$ .

### 3.3 Turbulence level and Reynolds stresses anisotropy

Some effects of thermal stratification on the turbulence field are shown in Fig. 8 for D4. Increase in the normalized turbulent kinetic energy with decrease in  $Ri_\tau$  is evident in Fig. 8a. The ratio of vertical to streamwise fluctuations in Fig. 8b is found to be nearly the same for neutral and unstable cases thus suggesting that this structural parameter is not affected by ground heating, at least within the range  $0 > Ri_\tau \geq -2$ . However, for the stable case at  $Ri_\tau = 2.5$  the ratio is found to be slightly larger than in the neutral and unstable cases. This indicates that the turbulence structural characteristics of the stable case are different to those of neutral and unstable cases. Therefore, further exploration of turbulence structure have been carried out and are discussed in the following paragraphs. Figure 8(c) shows that the normalized temperature fluctuations are almost constant throughout the domain height, except near the bottom and top surfaces where the temperature gradients are inevitably strongest because of proximity to the imposed boundary conditions.

The anisotropy of the time mean Reynolds stresses is often used as an indicator of turbulence structure and this is shown using Lumley's anisotropy invariant map, AIM (Pope, 2011). Figure 9 shows AIM for various  $Ri_\tau$  and for four typical locations, as identified by Castro et al. (2006) and indicated as  $P_{0-3}$  in Fig. 2. The AIM is obtained from the second and third principle invariants of the stress tensor  $b_{ij}$ ,  $6\eta^2 = -2II_b = b_{ij}b_{ji}$  and  $6\xi^3 = 3III_b = b_{ij}b_{jk}b_{ki}$ , where

$$b_{ij} = \frac{\langle \overline{u_i u_j} \rangle}{2k} - \frac{\delta_{ij}}{3}. \quad (19)$$

The vertical axis  $\eta$  of the AIM gives the magnitude of the anisotropy and the horizontal axis  $\xi$  represents the shape of anisotropy (i.e. distinguishing qualitatively between 'rod-like' and 'disc' shaped turbulent eddies). The linear sides of the triangle originating from  $(\xi, \eta) = (0, 0)$  represent axisymmetric turbulence and the origin indicates isotropy.  $\xi > 0$  implies 'rod-like' shaped turbulence where two eigenvalues of the Reynolds stress tensor are smaller than the third one and  $\xi < 0$  refers to 'disc'

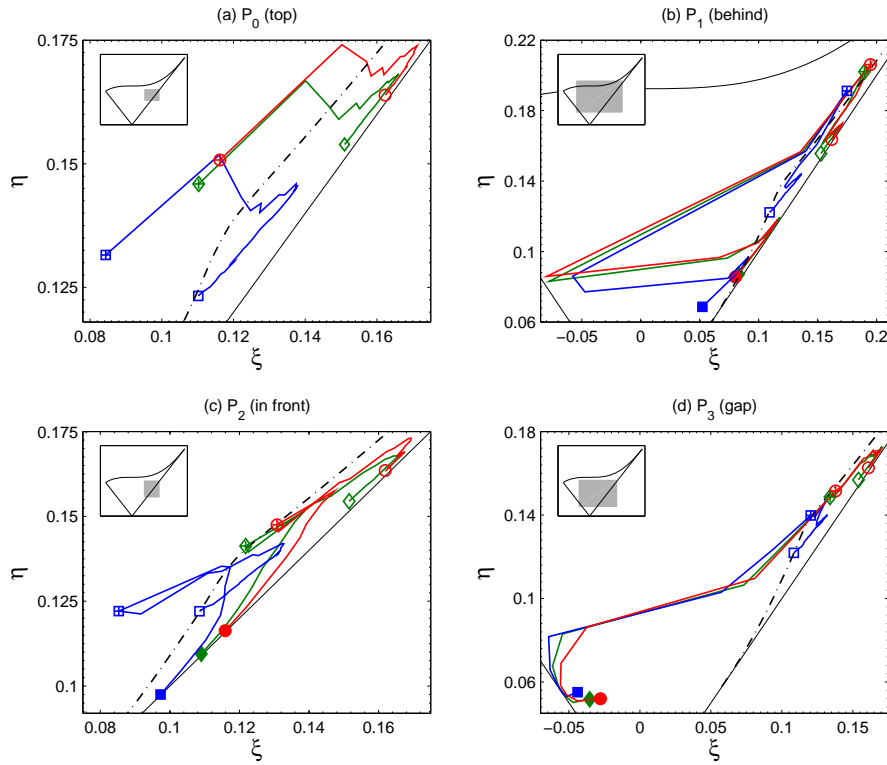


**Fig. 9** AIM at typical locations for  $Ri_\tau \approx -2$  (circles), 0 (diamonds) and 2.5 (squares). For clarity, only the immediate regions occupied by the data are shown, with solid black lines indicating boundaries of the Lumley triangle where appropriate; the inset figures show these regions in a grey shade, in relation to the entire Lumley triangle. Filled symbols are at  $z/h = 0.5$ , open symbols with an internal '+' are at  $z/h = 1$  and clear open symbols are at  $z/h = 3$ . The dash-dot line near the right outline of the Lumley triangle is the logarithmic and core region data ( $30 \leq z^+ \leq 180$ ) from smooth wall turbulent channel flow with  $Re_\tau = 180$  (Busse and Sandham, 2012); here the data approach  $(\xi, \eta) = (0, 0)$  with increasing distance from the wall.

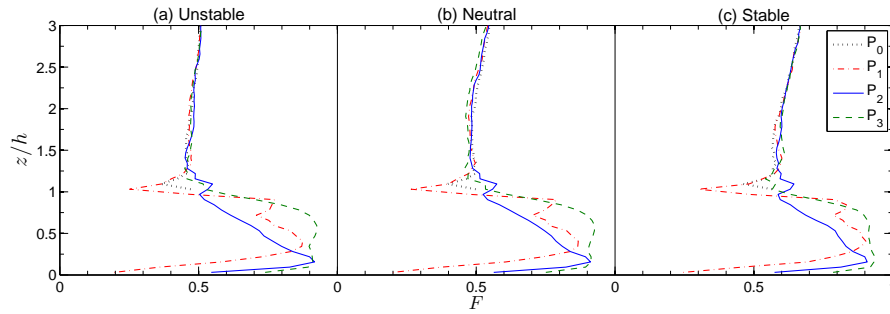


**Fig. 10** The anisotropy function for (a)  $Ri_\tau = -2$  (unstable), (b) 0 (neutral) and (c) 2.5 (stable) cases at typical locations.

361 shaped turbulence where two eigenvalues are greater than the third eigenvalue of the  
 362 Reynolds stress tensor. The upper curve of the triangle represents two-component  
 363 turbulence where one of the eigenvalues is zero.

364 For clarity, data within the AIM are shown only for  $0.5 \leq z/h \leq 3$  in Fig. 9. The  
 365 data shown at each typical location  $P_i$ , where  $i = 0-3$ , are temporal and spatial means  
 366 at the four identical locations in the computational domain. Comparison of AIM data  
 367 for  $P_1$  and  $P_2$  for  $Ri_\tau = 0$  with the experimental values of Castro et al. (2006) show  
 368 qualitative agreement (not shown here).

369 It is observed that the shapes of profiles for neutral and unstable cases are very  
 370 similar and they differ mostly in the magnitude of anisotropy. The structure of the  
 371 anisotropy for the stable case is found to be slightly different to that of neutral and  
 372 unstable cases. At all four typical locations, the magnitude of anisotropy is found  
 373 to be generally lower in a stable and higher in an unstable case, and this is very  
 374 evident in the profiles at  $P_0$  and  $P_2$ . For  $z/h > 1.2$  (i.e. in the log-linear region of  
 375 the mean velocity profile), the profiles at all four locations are on or close to the right  
 376 outline of the Lumley map just as they are in the log and core region of a smooth-wall  
 377 turbulent channel flow at  $Re_\tau = 180$  (Busse and Sandham, 2012). This suggests an  
 378 axisymmetric nature of turbulence with predominantly ‘rod-like’ shaped eddies. With  
 379 increasing  $z/h$  above the canopy the data tend to move towards the origin, just as they  
 380 do in the smooth-wall channel flow. However, note that, unlike the data in the neutral  
 381 and unstable cases that are very close to right outline of the Lumley map, stable case  
 382 data are a little further away from the right boundary. Overall, we conclude that even  
 383 with surface heating or cooling the turbulence structure in the log region (i.e. above  
 384 the urban canopy) is not very different to that in the log region of flow over smooth  
 385 surfaces. This indicates that for  $z/h > 1.2$ , the turbulent structure is similar to that of  
 386 smooth-wall boundary layer. The fact that in neutral flows urban-type roughness does  
 387 not have a large effect on turbulence structure at least qualitatively within the log law  
 388 has previously been noted by Coceal et al. (2006). Based on the field measurements,  
 389 same observation was made by Roth et al. (2013) and this is conceptually shown in  
 390 the Fig. 6 of their article. It is interesting that the same seems to be true for cases of  
 391 moderate ground heating or cooling. The data suggest that changes become apparent  
 392 soonest for stable cases but, in any case, one would not expect the same conclusion  
 393 to hold if  $Ri_\tau$  were to increase to very large magnitudes.

394 As expected, the shapes of profiles at the lower heights (between  $z/h = 0.5$  and  
 395 1.2) differ significantly at the various locations. At  $P_1$  and with  $z/h$  increasing from  
 396 0.5, the turbulence structure becomes more ‘disc’ shaped, which could be due to the  
 397 recirculation region, and again changes back to ‘rod-like’ shape as the profile reaches  
 398 the canopy height. With increasing  $z/h$  at  $P_2$ , the turbulence structure appears to drift  
 399 gradually away from the ‘rod-like’ shape and revert back to this shape for  $z/h > 1$ .  
 400 At  $P_3$ , where the mean flow field experiences ‘channeling’ effects, the presence of  
 401 side-walls appears to encourage the turbulence structure to be more ‘disc’ shaped,  
 402 which is counter-intuitive.

403 A direct measure of the degree of isotropy in the turbulence is provided by the  
 404 parameter  $F = 1 + II_b + 27III_b$ ;  $F = 0$  and 1 represents two-component and isotropic  
 405 turbulence respectively. The values of this parameter at the four typical locations and  
 406 for various  $Ri_\tau$  are shown in Fig. 10. As expected, the values of  $F$  vary considerably

below the canopy, but not above where the flow is essentially homogeneous in  $x$  and  $y$ . Owing to the strong three-dimensional effects, the turbulence below the canopy becomes increasingly isotropic as  $z$  approaches zero, especially at  $P_1$  and  $P_3$ , until very close to the wall when of course eddies are strongly constrained vertically. Such high values of  $F$  were also observed in the wind-tunnel experiments of Castro et al. (2006) for the neutral case. Perhaps surprisingly, the values of  $F$  below the canopy are found to be almost same for stable, neutral and unstable cases. This must be due to the very high turbulence intensities caused by shear and the wake of the cubes, which are not strongly reduced by surface heating or cooling. But above the canopy, the stable case shows slightly larger values of  $F$  compared to neutral and unstable cases.

The above analysis was also carried out for case D64 with  $Ri_\tau = 0$  and  $-2$ ; the corresponding figures (not shown here) show qualitatively similar behaviour to that for D4. Differences were most evident above the canopy, no doubt because of the non-zero dispersive stresses there.

### 3.4 Spatial correlations

In order to determine the influence of thermal stratification on the integral length scales of the turbulent structures, two-point velocity correlations were computed. The spatial correlation for streamwise velocity in the streamwise direction is given by (e.g. Castro et al., 2006)

$$R_{uu}(\Delta x) = \frac{\overline{u'(x)u'(x+\Delta x)}}{\overline{\sigma'_u(x)\sigma'_u(x+\Delta x)}}. \quad (20)$$

The two-point correlation of vertical velocity in the vertical direction is obtained by replacing  $u$  and  $x$  in Eq. (20) with  $w$  and  $z$  respectively. Figure 11 shows these computed correlations for D4; the streamwise spatial correlations are shown at  $z/h = 1.28$  and the vertical spatial correlations are obtained by specifying  $z/h = 1.53$  as a fixed reference. It is observed in this figure that  $R_{uu}(\Delta x)$  does not tend to zero at  $\Delta x = 2$ , which is half of the streamwise domain length. This suggests that the domain length is not sufficient to capture the longest eddy structures. Nonetheless, we can make some deductions from the data.

Figure 11 shows that  $R_{uu}(\Delta x)$  for the stable case is lower than that of the neutral and heated cases. The streamwise integral length scale has clearly been significantly reduced by ground cooling, but appears not to be influenced by ground heating. The reason for such a strong influence on streamwise length scales by stable stratification is not yet completely understood, although it is well known that stability generally weakens turbulence fields. The profiles of  $R_{ww}(\Delta z)$  indicate that the vertical integral length scales are marginally increased and decreased by ground heating and cooling respectively. This is expected because the size of the vertical structures is enhanced by thermal plumes due to buoyancy in an unstable case and reduced in the case of stable stratification. These spatial correlations suggest that the turbulent structures are smaller in stable stratification when compared to neutral and unstable cases. As smaller structures tend to be more isotropic, this observation is consistent with the



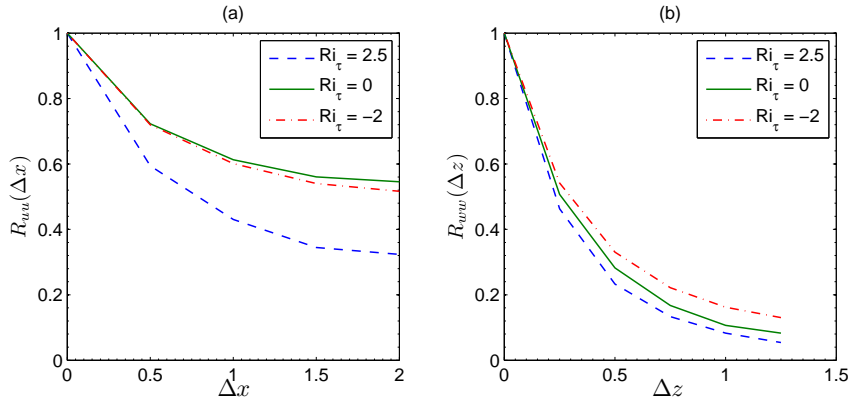


**Fig. 11** Spatial correlations of (a)  $u$  in  $x$  direction and (b)  $w$  in  $z$  direction for different  $Ri_\tau$ .

447 implications of the AIM discussed in Sect. 3.3. The spatial correlations from D64 for  
 448 neutral and unstable cases are, incidentally, found to be similar to those of D4.

### 449 3.5 Quadrant and Octant Analysis

450 The occurrence and contribution of various intermittent events to the transfer of mo-  
 451 mentum and heat is often deduced using quadrant analysis. According to this, the  
 452 events are classified as follows

$$\begin{aligned}
 \text{Q1: } & u' > 0, w' > 0; & \theta' > 0, w' > 0 \\
 \text{Q2: } & u' < 0, w' > 0; & \theta' < 0, w' > 0 \\
 \text{Q3: } & u' < 0, w' < 0; & \theta' < 0, w' < 0 \\
 \text{Q4: } & u' > 0, w' < 0; & \theta' > 0, w' < 0
 \end{aligned}
 \tag{21}$$

453 where primed quantities refer to fluctuating values (about their respective time-means).  
 454 In the case of momentum flux, ‘Q2’ refers to movement of low-speed fluid in the up-  
 455 ward direction (referred as ‘ejections’) and ‘Q4’ refers to movement of high-speed  
 456 fluid in the downward direction (referred as ‘sweeps’). In the case of stable stratifi-  
 457 cation, ‘Q2’ refers to those events where cold fluid moves in the upward direction  
 458 (termed as ‘updrafts’) and ‘Q4’ refers to those events where hot fluid moves in the  
 459 downward direction (termed as ‘downdrafts’). In the case of unstable stratification,  
 460 ‘Q1’ refers to ‘updrafts’ where hot fluid is ejected and ‘Q3’ refers to ‘downdrafts’  
 461 where cold fluid moves in the downward direction. The difference in the frequency  
 462 of occurrence of sweeps and ejections, and downdrafts and updrafts, and their pro-  
 463 portional contribution to total momentum and heat fluxes (often referred to as ‘flux  
 464 fraction’, but here we use the term ‘strength’) are shown in Fig. 12. The method used  
 465 to obtain the frequency and strength of momentum and heat flux for various events  
 466 is explained in detail in Boppana et al. (2013). The values shown in Figs. 12a, d are  
 467 obtained using a time average of  $330e_t$  and a spatial average of data at all the seven  
 468 locations shown as dots in Fig. 2 and identified as  $D_b$ ,  $D_i$  and  $D_g$ . The values shown

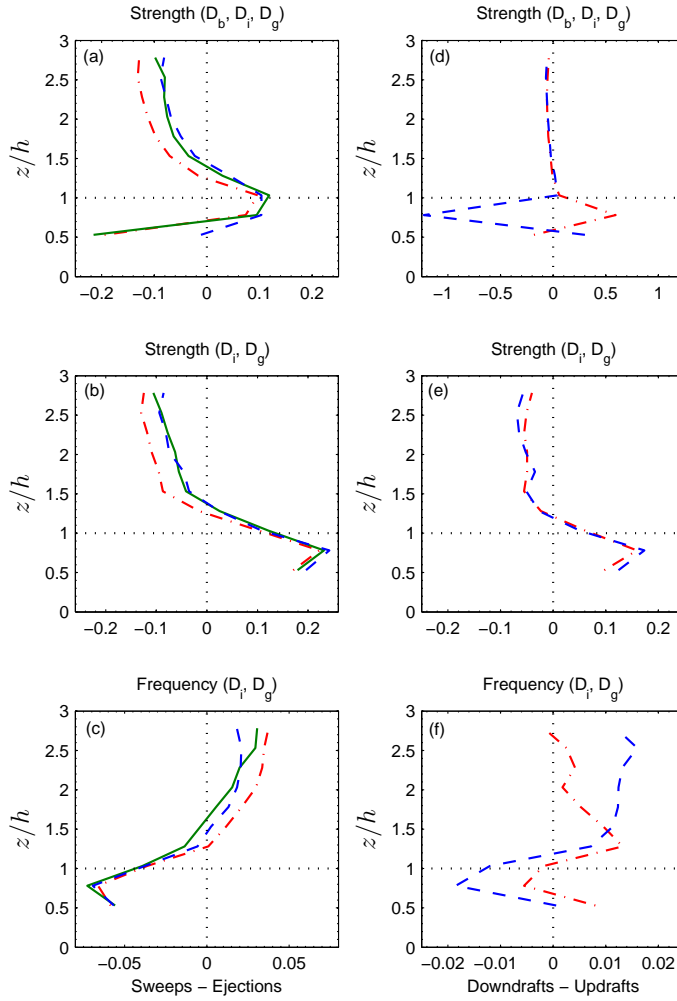


**Fig. 12** Left column: differences in the contributions to momentum flux by sweeps (Q4) and ejections (Q2) (a), (b) and the difference in their frequency of occurrence (c); right column: differences in the contributions to heat flux by downdrafts (Q4 - stable, Q3 - unstable) and updrafts (Q2 - stable, Q1 - unstable) (d), (e), and the difference in their frequency of occurrence (f). Dash-dot lines: unstable ( $Ri_\tau = -2$ ); solid lines: neutral ( $Ri_\tau = 0$ ); dash lines: stable ( $Ri_\tau = 2.5$ ). The time and spatial average of data from  $D_b$ ,  $D_i$  and  $D_g$  locations (shown in Fig. 2) are used in (a) and (d), and the average of data from  $D_i$  and  $D_g$  are used in (b), (c), (e) and (f).

469 in Figs. 12b, c, e and f are from a time and spatial average of the four locations  $D_i$   
 470 and  $D_g$  which do not lie in the recirculating regions immediately behind the cubes.

471 The time and spatial average of data from all seven locations shows that ejections  
 472 are stronger above the canopy (Fig. 12a), but below the canopy ejections dominate at  
 473  $z/h \approx 0.5$  whilst, for  $0.5 \leq z/h \leq 1$ , sweeps contribute more to the momentum flux.  
 474 Such a non-monotonic behaviour below the canopy is a result of the strong influence

475 of the recirculating region in the wake of the cubes. This influence is also observed  
 476 in the strength of events contributing to heat flux (Fig. 12d). As suggested in the  
 477 DNS study by Coceal et al. (2007), it is instructive to obtain the temporal and spatial  
 478 mean from all locations in the computational domain. But as the available data here  
 479 is limited to seven locations, the data from the three locations behind the cubes ( $D_b$ )  
 480 have been excluded in some of the results shown so as to prevent the strong influence  
 481 from the recirculation region biasing the results of the quadrant analysis. Figure 12b  
 482 then shows that momentum flux is dominated by sweeps below the canopy, which is  
 483 consistent with the observations made in the DNS study. (Including the three ‘behind  
 484 cube’ profile locations destroys that consistency.) Further analysis will therefore be  
 485 based on the time and spatial average data from the  $D_i$  and  $D_g$  locations only, shown  
 486 in Figs. 12b, c, e and f.

487 Below the canopy, the strength and frequency of momentum flux events in Figs.  
 488 12b,c are found to be the same for unstable, neutral and stable cases. This implies  
 489 that the mechanical turbulence generated by the roughness elements has a much  
 490 stronger influence than the local thermal stratification. Further above the canopy,  
 491 thermal stratification, especially for the unstable case, appears to have a notable ef-  
 492 fect as the strength of ejections and the frequency of sweeps is enhanced. In the field  
 493 study of Christen et al. (2007), point measurements from a tower in an urban street  
 494 canyon showed qualitatively similar behavior except that the strength of ejections be-  
 495 gins to dominate sweeps at  $z/z_h = 1.9$  for an unstable case and at  $z/z_h = 2.5$  for a  
 496 near-neutral case, whereas sweeps dominated throughout the measurement height i.e.  
 497  $0.5 \leq z/z_h \leq 2.5$  in the stable case ( $z_h$  is an average building height). The reason for  
 498 these minor differences between field experiments and LES could be partly attributed  
 499 to the urban morphometry, different  $Ri_\tau$ , prevailing meteorological conditions (e.g.  
 500 large-scale turbulent motions (Michioka et al., 2011) and wind direction) in the field.

501 Similar to the momentum flux contributions in stable and unstable cases, down-  
 502 drafts contribute more to the heat flux below the canopy and updrafts are stronger  
 503 above the canopy. Figure 12f suggests the reverse behaviour in the frequency of  
 504 events. The field study of Christen et al. (2007) showed similar behaviour in the  
 505 strength of events, but the stratification effects were found to be strong above the  
 506 canopy unlike this study, probably for reasons similar to those mentioned above.

507 The same analysis was carried out on time series data corresponding to a duration  
 508 of  $2000e_t$  and from eight locations situated in front of the cubes in D64. The strength  
 509 and frequency of events were found to be qualitatively very similar to those described  
 510 above for the D4 domain.

511 From the above analysis, it is understood that for both stable and unstable cases,  
 512 above the canopy ejections and updrafts contribute more to the momentum flux and  
 513 heat flux respectively, whereas within the canopy sweeps and downdrafts dominate.  
 514 Sweeps and downdrafts occur more often above the canopy, whilst ejections and up-  
 515 drafts are more frequent within the canopy. But it is not immediately clear if the  
 516 updraft (downdraft) and ejection (sweep) events are correlated. Inagaki et al. (2012)  
 517 showed that the horizontal distribution of ejection and sweep events at the building  
 518 height is similar to the distribution of updraft and downdraft events suggesting that  
 519 these events might be correlated. To determine this quantitatively, octant analysis (as  
 520 used by Dupont and Patton, 2012, on a vegetation canopy) has been conducted. Based

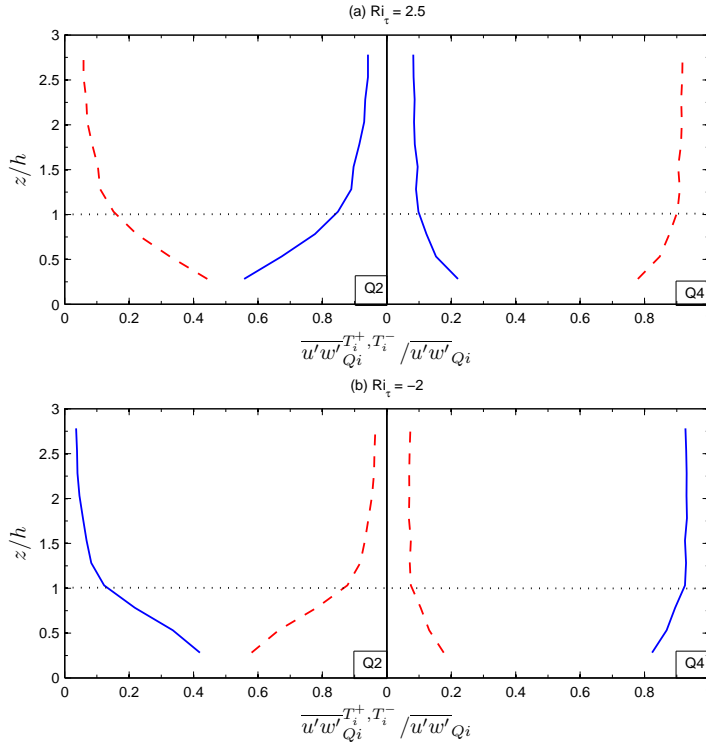


**Fig. 13** Momentum flux associated with positive (dashed line) and negative (positive line) temperature fluctuations in quadrants 2 and 4 for (a) stable and (b) unstable cases. The dotted line indicates the canopy top.

521 on the sign of temperature fluctuations, the momentum flux from a quadrant ‘ $Q_i$ ’ is  
 522 split further such that

$$\overline{(u'w')}_{Q_i} = \overline{(u'w')}_{Q_i}^{T_i^+} + \overline{(u'w')}_{Q_i}^{T_i^-}, \quad (22)$$

523 where  $T_i^+$  and  $T_i^-$  correspond to positive and negative temperature fluctuations re-  
 524 spectively in the quadrant  $Q_i$ . The two right hand terms in the above equation are  
 525 normalized with their respective quadrant momentum fluxes and are shown in Fig. 13.  
 526 For both stable and unstable cases the ‘updrafts’ contribution to the momentum flux  
 527 is found to be larger in ‘Q2’ and the ‘downdrafts’ contribution is found to be larger  
 528 for ‘Q4’. This suggests that updrafts (downdrafts) and ejections (sweeps) are well  
 529 correlated, which implies at least some degree of similarity in momentum and heat  
 530 transport for such flows.

---

## 531 4 Conclusions

532 The effects of local thermal stratification on the atmospheric flow in and above urban  
533 canopies have been investigated by conducting large-eddy simulations on flow past  
534 an array of staggered cubes, with the ground surface subjected to uniform cooling or  
535 heating. The global thermal influences have been quantified by computing drag and  
536 heat transfer coefficients. With increase in ground surface heating, characterised by  
537  $-23 < Ri_\tau < -0.2$ , a gradual increase in  $C_d$  and  $C_h$  was observed. Specification of  
538 either constant heat flux or constant temperature boundary condition on the ground  
539 surface yielded similar values of  $C_d$  and  $C_h$ , despite the different physics of flow  
540 and heat very close to the ground surface. With increase in ground surface cooling,  
541 i.e.  $0 < Ri_\tau < 9$ , a gradual decline in  $C_d$  and  $C_h$  was observed. The steady increase  
542 in  $C_d$  and  $C_h$  with decrease in  $Ri_\tau$  is linked with an increase in turbulent kinetic  
543 energy due to buoyancy. The sensitivity tests included computations with different  
544 domain sizes, grid resolution and means of achieving the steady state for energy in  
545 the computational domain. These showed that  $C_d$  was relatively insensitive to all  
546 these, but the estimates of  $C_h$  were found to be very sensitive to resolution in the  
547 near-wall region, not surprisingly.

548 The structure of the turbulence for  $Ri_\tau = -2, 0$  and  $2.5$  was then quantitatively  
549 analysed by exploring the Reynolds stresses, spatial correlations and the results of  
550 quadrant and octant analyses. The turbulence intensity was found to be significantly  
551 affected by ground heating and cooling. However, the anisotropy invariant maps implied  
552 that the shape of the turbulent structures remained very similar for neutral and  
553 unstable cases, but differed slightly in the stable case. From the two-point spatial  
554 correlations it was observed that the turbulent integral length scales of the structures  
555 are reduced in both streamwise and vertical directions by stable stratification when  
556 compared to the neutral case; only the vertical integral length scale was found to  
557 be increased by ground heating. The quadrant analysis showed that ground heating  
558 (cooling) enhances (reduces) the contribution of ejections to momentum flux above  
559 the canopy whereas the contribution of updrafts and downdrafts to heat flux are found  
560 to be very similar. Octant analysis showed that the strength of ejections (sweeps) and  
561 updrafts (downdrafts) are well correlated, thereby suggesting that the transport mechanisms  
562 of momentum and heat flux are similar above the canopy, probably because of  
563 the prevailing large-scale structures although no attempt has yet been made to study  
564 the correlated spectral content between ejections and updrafts in order to delineate  
565 scale effects.

566 This study has shed some light on the effects of local thermal stratification on  
567 the aerodynamic coefficients and turbulent structure of flow over an idealised urban  
568 canopy. It would be useful to know whether the general conclusions outlined above  
569 apply also to different kinds of roughness morphology, and to what extent they are  
570 affected by differential surface heating arising for example from radiation. Coupled  
571 with the present results, this might then be a further step towards understanding and  
572 modelling the pollutant dispersion in significantly non-neutral urban boundary layers.

573 **Acknowledgements** This project is funded by the Natural Environment Research Council, through its  
574 National Centre for Atmospheric Sciences, Grant No. R8/H12/38. All computations have been done using

575 CD-adapco's STAR-CD code on Iridis (University's supercomputer) and HECToR (U.K.'s supercomputer).  
576 We thank the CD-adapco's staff Fred Mendonca for his continuous support.

## 577 References

- 578 Allegrini J, Dorer V, Carmeliet J (2013) Wind tunnel measurements of buoyant flows  
579 in street canyons. *Build Environ* 59:315–326
- 580 Armenio V, Sarkar S (2002) An investigation of stably stratified turbulent channel  
581 flow using large-eddy simulation. *J Fluid Mech* 459:1–42
- 582 Boppa VBL, Xie ZT, Castro IP (2010) Large-eddy simulation of dispersion from  
583 surface sources in arrays of obstacles. *Boundary-Layer Meteorol* 135:433–454
- 584 Boppa VBL, Xie ZT, Castro IP (2013) Large-eddy simulation of heat transfer from  
585 a single cube mounted on a very rough wall. *Boundary-Layer Meteorol* 147:347–  
586 368
- 587 Britter RE, Hanna SR (2003) Flow and dispersion in urban areas. *Annu Rev Fluid*  
588 *Mech* 35:469–496
- 589 Busse A, Sandham ND (2012) Parametric forcing approach to rough-wall turbulent  
590 channel flow. *J Fluid Mech* 712:169–202
- 591 Cai X (2012) Effects of differential wall heating in street canyons on dispersion and  
592 ventilation characteristics of a passive scalar. *Atmos Environ* 51:268–277
- 593 Castro IP, Cheng H, Reynolds R (2006) Turbulence over urban-type roughness: de-  
594 ductions from wind-tunnel measurements. *Boundary-Layer Meteorol* 118:109–  
595 131
- 596 Cheng H, Castro IP (2002) Near wall flow over urban-like roughness. *Boundary-*  
597 *Layer Meteorol* 104:229–259
- 598 Cheng WC, Liu CH (2011) Effect of unstable thermal stratification on the atmo-  
599 spheric boundary layer above urban street canyons by large-eddy simulation.  
600 The 14<sup>th</sup> International conference on harmonisation within atmospheric dispersion  
601 modelling for regulatory purposes (HARMO14), Kos, Greece, 2–6 October
- 602 Christen A, van Gorsel E, Vogt R (2007) Coherent structures in urban roughness  
603 sublayer turbulence. *Int J Climatol* 27:1955–1968
- 604 Coceal O, Thomas TG, Castro IP, Belcher SE (2006) Mean flow and turbulence  
605 statistics over groups of urban-like cubical obstacles. *Boundary-Layer Meteorol*  
606 121:491–519
- 607 Coceal O, Dobre A, Thomas TG, Belcher SE (2007) Structure of turbulent flow over  
608 regular arrays of cubical roughness. *J Fluid Mech* 589:375–409
- 609 Dong YH, Lu XY (2005) Direct numerical simulation of stably and unstably stratified  
610 turbulent open channel flows. *Acta Mech* 177:115–136
- 611 Dupont S, Patton EG (2012) Momentum and scalar transport within a vegetation  
612 canopy following atmospheric stability and seasonal canopy changes: the chats  
613 experiment. *Atmos Chem Phys* 12:5913–5935
- 614 Fishpool GM, Lardeau S, Leschziner MA (2009) Persistent non-homogeneous fea-  
615 tures in periodic channel-flow simulations. *Flow Turbulence Combust* 83:323–342
- 616 Gao W, Shaw RH, Pawu KT (1989) Observation of organized structure in turbulent  
617 flow within and above a forest canopy. *Boundary Layer Meteorol* 47:349–377

- 618 García-Villalba M, del Álamo J (2011) Turbulence modification by stable stratifica-  
619 tion in channel flow. *Phys Fluids* 23:045,104–22
- 620 Huizhi L, Bin L, Fengrong Z, Boyin Z, Jianguo S (2003) A laboratory model for  
621 the flow in urban street canyons induced by bottom heating. *Adv Atmos Sciences*  
622 20:554–564
- 623 Inagaki A, Castillo MCL, Yamashita Y, Kanda M, Takimoto H (2012) Large-eddy  
624 simulation of coherent flow structures within a cubical canopy. *Boundary-Layer*  
625 *Meteorol* 142:207–222
- 626 Jackson PS (1981) On the displacement height in the logarithmic velocity profile. *J*  
627 *Fluid Mech* 111:15–25
- 628 Jayatilaka CL (1969) The influence of prandtl number and surface roughness on the  
629 resistance of the laminar sub-layer to momentum and heat transfer. *Progress in heat*  
630 *and mass transfer* 1:193–330
- 631 Kaimal JC, Finnigan JJ (1994) *Atmospheric Boundary Layer Flows: Their Structure*  
632 *and Measurement*. Oxford University Press, 304 pp
- 633 Kanda M, Kanega M, Kawai T, Moriwaki R (2007) Roughness lengths for momen-  
634 tum and heat derived from outdoor urban scale models. *J Applied Meteorol and*  
635 *Climatol* 46:1067–1079
- 636 Kim JJ, Baik JJ (1999) A numerical study of thermal effects on flow and pollutant  
637 dispersion in urban street canyons. *J App Meteorol* 38:1249–1261
- 638 Kovar-Panskus A, Moulinneuf L, Savory E, Abdelqari A, Sini JF, Rosant JM, Robins  
639 A, Toy N (2002) A wind tunnel investigation of the influence of solar-induced wall-  
640 heating on the flow regime within a simulated urban street canyon. *Water, Air, and*  
641 *Soil Pollution: Focus* 2:555–571
- 642 Leonardi S, Castro IP (2010) Channel flow over large cube roughness: a direct nu-  
643 merical simulation study. *J Fluid Mech* 651:519–539
- 644 Li D, Bou-Zeid E (2011) Coherent structures and the dissimilarity of turbulent  
645 transport of momentum and scalars in the unstable atmospheric surface layer.  
646 *Boundary-Layer Meteorol* 140:243–262
- 647 Michioka T, Sato A, Sada K (2011) Wind-tunnel experiments for gas dispersion in  
648 an atmospheric boundary layer with large-scale turbulent motion. *Boundary-Layer*  
649 *Meteorol* 141:35–51
- 650 Park SB, Baik JJ, Raasch S, Letzel MO (2012) A large-eddy simulation study of  
651 thermal effects on turbulent flow and dispersion in and above a street canyon. *J*  
652 *Appl Meteorol and Climatol* 51:829–841
- 653 Pascheke F, Barlow JF, Robins A (2008) Wind-tunnel modelling of dispersion from  
654 a scalar area source in urban-like roughness. *Boundary-Layer Meteorol* 126:103–  
655 124
- 656 Pope SB (2011) *Turbulent flows*. Cambridge University Press, 774 pp
- 657 Richards K, Schatzmann M, Leitl B (2006) Wind tunnel experiments modelling the  
658 thermal effects within the vicinity of a single block building with leeward wall  
659 heating. *J Wind Eng Ind Aerodyn* 94:621–636
- 660 Roth M, Inagaki A, Sugawara H, Kanda M (2013) Small-scale spatial variability of  
661 turbulent statistics, (co)spectra and turbulent kinetic energy measure over a regular  
662 array of cube roughness. *Environ Fluid Mech* DOI 10.1007/s10652-013-9322-3

- 663 Shih TH, Povinelli LA, Liu NS, Potapczuk MG, Lumley JL (1999) A generalized  
664 wall function. Tech. rep., National Aeronautics and Space Administration
- 665 STAR-CD (2007) CD-adapco's CCM methodology, STAR-CD Version 4.04, 328 pp
- 666 Stull RB (2009) An introduction to Boundary-Layer Meteorology. Springer, 674 pp
- 667 Uehara K, Murakami S, Oikawa S, Wakamatsu S (2000) Wind tunnel experiments on  
668 how thermal stratification affects flow in and above urban street canyons. *Atmos*  
669 *Environ* 34:1553–1562
- 670 Xie ZT, Hayden P, Wood CR (2013) Large-eddy simulation of approaching-flow  
671 stratification on dispersion over arrays of buildings. *Atmos Environ* 71:64–74